Metal–Insulator Transition and Magnetic Properties of La$_{1-x}$Eu$_x$NiO$_3$ (0 ≤ x ≤ 1)

R. D. Sánchez[1,2] and M. T. Causa

Centro Atómico Bariloche and Instituto Balseiro, Universidad Nacional de Cuyo, 8400-S.C. de Bariloche, Argentina

A. Seoane and J. Rivas

Departamento de Física Aplicada, Universidad de Santiago de Compostela, 15706-Santiago de Compostela, Spain

F. Rivadulla and M. A. López-Quintela

Departamento de Química-Física, Universidad de Santiago de Compostela, 15706-Santiago de Compostela, Spain

and

J. J. Pérez Cacho, J. Blasco, and J. García

Instituto de Ciencia de Materiales de Aragón, Departamento de Física de la Materia Condensada, Universidad de Zaragoza, 500009-Zaragoza, Spain

This paper reports X-ray diffraction patterns, Rietveld fit profiles, electrical resistivity dc magnetic susceptibility, and electron paramagnetic resonance (EPR) measurements of La$_{1-x}$Eu$_x$NiO$_3$ (0 ≤ x ≤ 1). A shift to high temperature of the metal–insulator transition temperature with x and hysteresis in the electrical resistivity and magnetization versus temperature at intermediate concentration of the compound are observed. The antiferromagnetic order of the Ni sublattice can be observed after subtracting the magnetic contribution of the rare earth ions. A change in space group from **R-3c** to **Pbnm** for x ≥ 0.4 was detected, as was the appearance of magnetic order. Samples with 1% Gd^{3+} probe were studied by EPR. Drastic changes were observed in the shape of the lines with x, though the crystal field symmetry of the Gd sites remained constant in all the samples studied. We observed that when Eu substitution increases, the number of Gd ions that contribute to the crystal-field spectrum diminishes. A possible cause of this effect is a previously reported increase in the Ni–O covalence in the neighborhood of the Eu sites. © 2000 Academic Press

Key Words: metal insulator transition; perovskite; electron paramagnetic resonance; magnetic susceptibility.

[1]Member of Carrera de Investigador CONICET (Argentina).
[2]To whom correspondence should be addressed. Fax: +54-2944-445299. E-mail: rodo@cab.cnea.gov.ar.

1. INTRODUCTION

RNiO$_3$ oxides (R = rare earth) provide an excellent opportunity to study the correlation between structural changes and electric and magnetic properties. These oxides present a sharp metal-to-insulator transition related to the distortion induced in the ideal cubic pervoskite structure.

In the perovskite structure, regular NiO$_6$ octahedra share corners to form a three-dimensional array, with the R ions occupying the space between these octahedra. The $x = 0$ member of the La$_{1-x}$Eu$_x$NiO$_3$ series, LaNiO$_3$ (1), is a metallic compound, but when the rare-earth radius decreases, the compounds show a metal–insulator transition, the temperature of which increases. The diminution in the rare-earth radius distorts the perovskite ideal cubic structure by tilting the NiO$_6$ octahedra and then reducing the Ni–O–Ni angle (2). Since the electronic bandwidth and the magnetic exchange interaction are closely related to the cosine of the Ni–O–Ni bond angle (2), a comparison between this parameter, which was obtained by the Rietveld refinement, and the electrical behavior was made.

Zaanen, Sawatzky, and Allen (ZSA) (19) developed a general model for oxides, accounting for differences between metallic and insulating conductivity or a great number of oxides. In this model, not only do transition metal bands determine metal or insulating behavior, but the 2p-oxygen band plays an important role in electrical properties of this type of oxides as well. Moreover, the position of the valence

oxygen band in relation to Ni bands can lead metal or insulating states.

If oxygen and conduction metal bands overlap, the metal state appears. Otherwise, the compound is an insulator, and two types of energy gap are possible:

(1) a Mott–Hubbard gap, related to the Coulomb correlation energy (U) between the metal bands;

(2) a change-transfer gap, dominated by the energy difference between $2p$ oxygen and conduction metal bands (Δ-W).

$RNiO_3$ compounds are charge-transfer insulators and the metal–insulator transition arises from the disappearance of the energy gap, as a consequence of increasing bandwidth. Here, we describe variations in the structure when europium replaces lanthanum and the relation with the metal–insulator transition, in the context of the ZSA model.

Two additional aspects should, however, be taken into account. One of them is the recently observed ^{16}O–^{18}O isotope shift in the metal–insulator transition temperature for $RNiO_3$ perovskites, indicating that the mechanism of transition involves a strong electron–lattice interaction (3). More recently, changes in the crystal symmetry at the metal–insulator transition in $YNiO_3$ perovskite have been observed (4). In this second aspect, the authors propose that this change is due to charge disproportionation ($2Ni^{3+} \rightarrow Ni^{3+\delta} + Ni^{3-\delta}$) that develops at the gap opening.

This paper also presents a study of the magnetic properties of the $La_{1-x}Eu_xNiO_3$ series. To discuss the effects of tolerance factor and rare-earth nature on the antiferromagnetic (AF) interactions in the Ni sublattice, the results of two different experiments are presented: (a) measurements of dc susceptibility (χ_{dc}) in the paramagnetic (PM) regime (From these data, the susceptibility corresponding to the Ni sublattice is derived as a function of T and x; (b) measurements of electron paramagnetic resonance (EPR) in $La_{1-x}Eu_xNiO_3$ doped with Gd^{3+} ions (1%) performed at low temperature. These data are discussed taking into account the results of neutron diffraction experiments (5, 6).

2. EXPERIMENTAL DETAILS

Samples were prepared using a citrate route and thermal treatment under an oxygen pressure of 200 bar. Stoichiometric amounts of La_2O_3, Eu_2O_3 (or Gd_2O_3), and $2NiCO_2 \cdot 3Ni(OH)_2 \cdot 4H_2O$ were dissolved in nitric acid. After addition of citric acid and ethylene glycol in the appropriate ratio (7), the solutions were heated until gels formed. These gels were dried to obtain brown powders which calcined overnight by immersion in oxygen flowing at 500°C. The resulting black powders were pressed (4–5 kbar) and sintered at 900°C, under oxygen pressure of 200 bar for 12 h. This batch of samples was called Series A. An other batch was prepared under the same conditions, Series B, where 1% Gd replaced the same percentage of Eu ($La_{1-x}Eu_{x-0.01}Gd_{0.01}NiO_3$) in all the samples. The Gd is

introduced as a probe to study, by EPR technique, the interaction between Gd spins and the crystal field near the metal–insulator transition temperature. We expect that the influence of this small Gd^{+3} concentration on the electrical and magnetic properties of our samples is negligible.

X-ray powder diffraction (XRD) patterns were collected using a $\theta/2\theta$ scan with $CuK\alpha$ radiation and a Phillips PW1710 system, operating at 40 kV and 30 mA at room temperature. For the structural refinement, the diagrams were obtained by step-scanning from 12° up to 100° with a step size of 0.02° and a counting time of 10 s/step. XRD patterns were analyzed by the Rietveld method with the FULLPOF program. A Thompson–Cox–Hastings pseudo-Voigt function was used as the diffraction peak shape, and a March–Dollase function as the preferred orientation function. No regions were excluded in the refinement. The following parameters were refined for each phase: background, zero point, half-width, asymmetry, and preferred orientation parameters for the peak shape; scale factor, and positional and unit cell parameters for the structural model.

Electrical resistance was measured by a standard dc four-probe method in the temperature range 77–460 K. Data were taken by increasing and decreasing temperature at the rate of 1 K/min. To improve experimental accuracy, the measurements were performed with a constant electrical current intensity covering the range from microamperes to milliamperes. For these experiments, pellets were cut in a bar shape and ρ were calculated taking into account geometric factors. Electrical contacts were made with Au sputtering over the samples.

Magnetization as a function of temperature at $H = 5$ kOe was measured at $5 \leq T$ (K) ≤ 300 with a superconducting quantum interference device (SQUID) magnetometer and at $300 \leq T$ (K) ≤ 600 with a vibrating sample magnetometer (VSM). In both cases the suceptibility was computed as M/H.

EPR spectra were taken at 9.5 GHz (X-Band) between 4 and 300 K with a Bruker ESP-300 spectrometer.

3. EXPERIMENTAL RESULTS

a. Structural Characterization

In Fig. 1 XRD patterns of $La_{1-x}Eu_xNiO_3$ are shown. Small amounts of an impurity phase (NiO) were detected only for $x = 1$ and $x = 0$ samples, but they are negligible for the results of the refinement. For $x < 0.4$, XRD patterns can be described with a rhombohedral symmetry (space group R-$3c$). When $x \geq 0.4$ additional peaks are observed. These peaks are typical of an orthorhombically distorted perovskite structure (space group $Pbnm$).

For rhombohedral samples, atoms are placed at the following Wyckoff positions: R ($R = $ La, Eu, and Gd) at $6a$ (0, 0, 1/4), Ni at $6b$ (0, 0, 0), and O at $18e$ (x, 0, 1/4). Isotropic

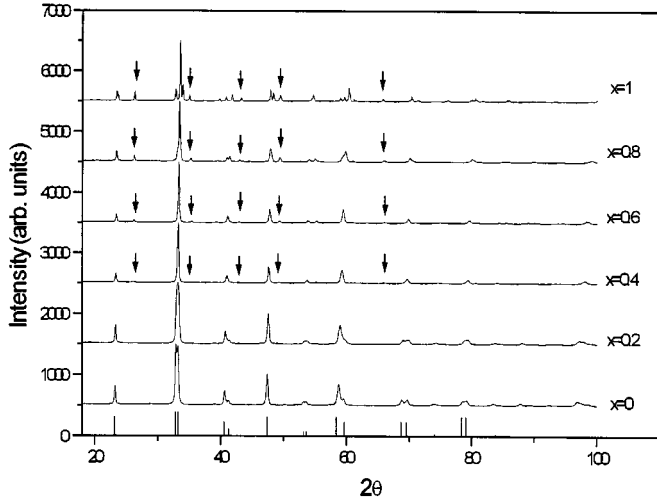**FIG. 1.** Powder diffraction patterns for the La$_{1-x}$Eu$_x$NiO$_3$ series. Arrows indicate extra peaks due to the orthorhombic distortion. At the bottom the expected LaNiO$_3$ diffraction lines can be seen.

thermal factors were set at 0.3, 0.21, and 0.55 Å^2 for rare earths, nickel, and oxygen, respectively.

For orthorhombic samples, rare earths are placed at $4c$ (x, y, 1/4); nickel at $4b$ (1/2, 0, 0) and there are two nonequivalent positions for oxygen atoms: O$_I$ at $4c$ and O$_{II}$ at $8d(x, y, z)$. Isotropic thermal factors are 0.3 Å^2 for rare earth and nickel atoms and 0.7 Å^2 for oxygen atoms.

The structural refinement was performed taking as starting parameters those of the LaNiO$_3$ structure for samples with $x \leq 0.4$ (20) and those of EuNiO$_3$ for samples with $x > 0.4$ (8).

Figure 2 shows the refined diffraction patterns for La$_{0.8}$Eu$_{0.2}$NiO$_3$ and La$_{0.6}$Eu$_{0.4}$NiO$_3$ samples. The refined structural parameters, i.e., unit cell parameters and atomic positions, are listed in Table 1, together with conventional Rietveld reliability factors.

Unit cell parameters for $x = 0$ and $x = 1$ are in excellent agreement with those values reported for LaNiO$_3$ (20) and EuNiO$_3$ (8).

As the lanthanum content increases, so does the unit-cell volume, due to the larger atomic radius of lanthanum. The Ni–O distances and Ni–O–Ni angle obtained for the series studied are listed in Table 2, as is the tolerance factor.

The Ni–O distance (d$_{Ni-O}$) remains practically unchanged all through the series, whereas the rare-earth distance (d$_{R-O}$) decreases with europium content. This fact suggests that distortion in the perovskite structure is caused by a tilt of NiO$_6$ octahedrons, not by their deformation. An estimation of this rotation can be made using the Ni–O–Ni angle. When Eu replaces La we observe that this angle decreases from 165.1° to 151.0° for LaNiO$_3$ to EuNiO$_3$, respectively.

b. Electrical Resistivity

Figure 3 shows how the resistivity of the La$_{1-x}$Eu$_x$NiO$_3$:Gd^{3+} Series B varies with temperature in the range $77 \leq T(K) \leq 460$. Also shown is the resistivity of Series A samples without gadolinium.

While LaNiO$_3$ remains metallic between 77 and 460 K, a metal–insulator (M–I) transition, T_{M-I}, appears with the decreasing size of the rare-earth ion (2). The resistivity increases below transition temperature by several orders of magnitude and a large thermal hysteresis (~ 40 K) can be observed when the samples become insulating at intermediate x values. In these cases the M–I transition temperature was taken as the average value between the cooling and heating curves. Samples with $x = 0.4$, 0.5, 0.6, and 0.8 show this sharp M–I transition (Fig. 3) at 125, 190, 260, and 380 K respectively.

We do not appreciate significant changes in the characteristics of the electrical resistivity when 1% Eu is replaced by 1% Gd. Both samples show similar semiconducting behavior at low temperatures with thermal hysteresis (same width) and metallic behavior at high temperatures (see case of $x = 0.6$ in Fig. 3).

For EuNiO$_3$ ($x = 1$ case), we do not observe the M–I transition in this temperature range but it was reported at 460 K in Ref. (8).

The T_{M-I} data obtained increase linearly with Eu content (x) at the rate of about 560 K/x; assuming this, we can estimate $T_{M-I} \sim 30$ K for the sample with $x = 0.2$.

For samples showing semiconduting behavior ($d\rho/dT < 0$) and no hysteresis for a range of temperature ($x = 0.8$ and $x = 1$), resistivity can be approximated by means of the general relationship (Mott's law)

$$\rho(T) = \rho_0 f(T) e^{(T_0/T)^p}, \qquad [1]$$

where $f(T)$ is the T dependence of the preexponential factor and the p value determines the electrical resistivity behavior. The temperature dependence $[f(T)]$ of the preexponential factor in semiconductors is usually negligible or in some cases is expressed as $T^{1/2}$ or T. If $p = 1$, then we can estimate the energy gap between the conduction and valence bands (E_a). The resistivity versus temperature curve in the $x = 1$ sample can be reasonably well fitted supposing this simple activated behavior. We obtained an activation energy of 22.0(3) meV between 77 and 130 K (see A in Fig. 4), or 36.0(2) meV, in the temperature range 130–240 K (B in Fig. 4). These values are within the range of those obtained for similar compounds, like PrNiO$_3$ (22 meV) and NdNiO$_3$ (25 meV) (9).

A thermally activated hopping mechanism can be present, however. For this mechanism, called variable range hopping (VRH), $p = 1/(1 + D)$, where D is the electrical dimension of the compound. In La$_{1-x}$Eu$_x$NiO$_3$ $D = 3$ and
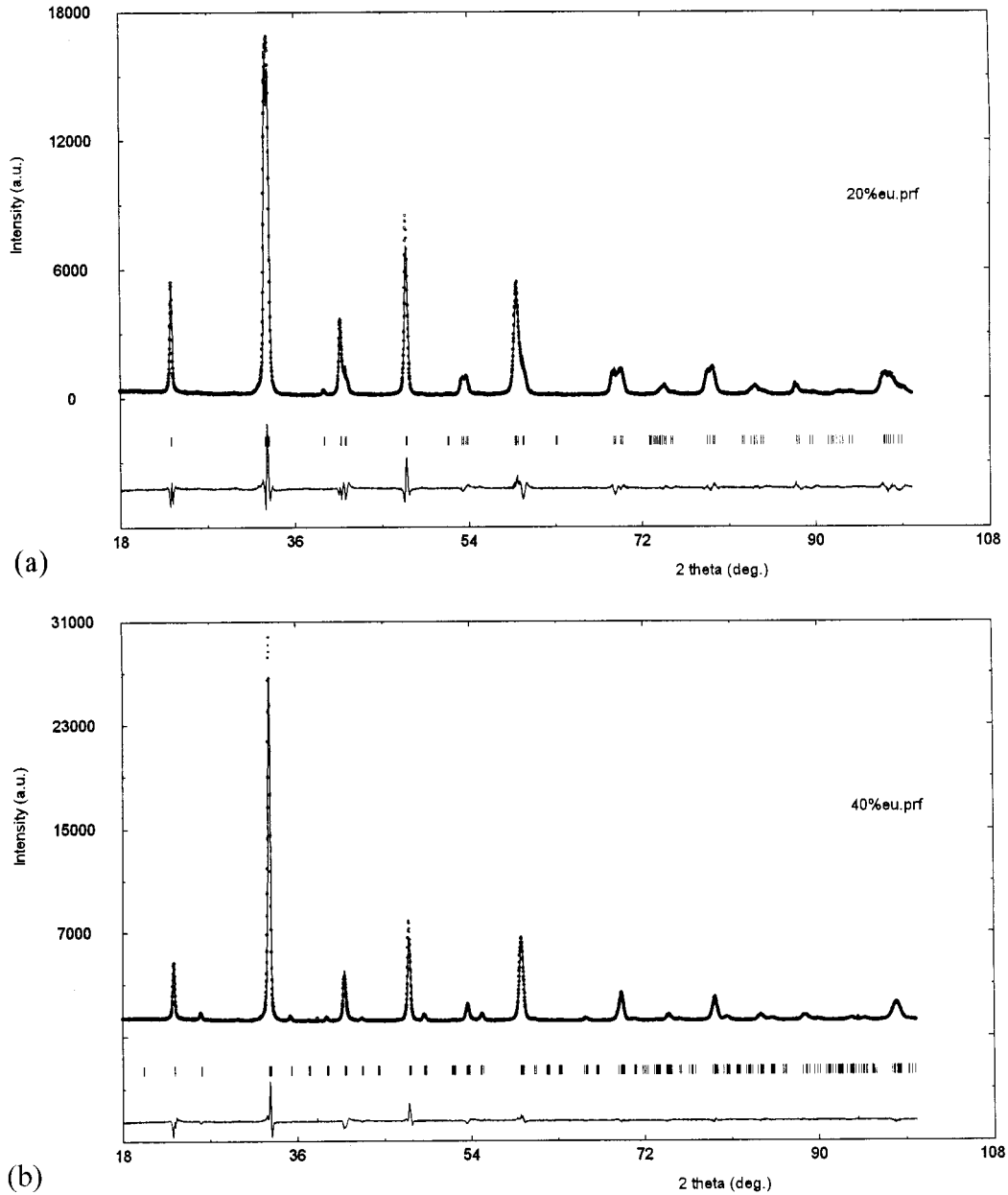
FIG. 2.   Rietveld refined XRD patterns for (a) $La_{0.8}Eu_{0.2}NiO_3$ (space group $R\text{-}3c$) and (b) $La_{0.6}Eu_{0.4}NiO_3$ (space group $Pbnm$).

in the VRH regime $p = 1/4$. This VRH mechanism is usually observed only at low enough temperatures. In some cases, a VRH dependence is observed at high temperatures, above half the Debye temperature, and is explained by polaron hopping (10). The $EuNiO_3$ sample could be described by a VRH model in the temperature range 77–300 K (C in Fig. 4) with a $T_0 = 1.553(4)\ 10^6$ K. For the $x = 0.8$ sample, this fit is valid from 77 to 175 K. Furthermore, for these samples the preexponential factor is temperature independent. This last polaronic conduction mechanism seems to be the predominant mechanism in the insulating samples in the speci-fied temperature range, showing an important electron–lattice interaction.

c. Magnetic Properties

$RNiO_3$ compounds have been included in a phase diagram by Torrance *et al.* (2) where Ni sublattice orders antiferromagnetically at $T_N = T_{M-I}$ for Nd and larger ions, and at $T_N < T_{M-I}$ for smaller rare-earths ions as in the case of $EuNiO_3$. This is an antiferromagnetic solid with $T_N = 205$ K and $T_{M-I} = 460$ K.

TABLE 1
Refined Fractional Atomic Positions, Unit Cell, Volume and Reliability Factors (%) for La$_{1-x}$Eu$_x$NiO$_3$ at Room Temperature

La$_{1-x}$Eu$_x$NiO$_3$:	$x = 0$	$x = 0.2$	$x = 0.4$	$x = 0.6$	$x = 0.8$	$x = 1$
Space group:	R-3c	R-3c	Pbnm	Pbnm	Pbnm	Pbnm
R						
X	—	—	0.995(1)	0.994(1)	0.991(1)	0.987(1)
Y	—	—	0.026(1)	0.036(1)	0.046(1)	0.057(1)
O(I)						
X	0.546(1)	0.550(2)	0.059(3)	0.057(3)	0.082(2)	0.082(2)
Y	—	—	0.486(1)	0.484(1)	0.483(1)	0.479(1)
O(II)						
X	—	—	0.709(1)	0.717(1)	0.717(1)	0.705(1)
Y	—	—	0.266(2)	0.292(1)	0.293(1)	0.302(1)
Z	—	—	0.033(2)	0.041(1)	0.043(1)	0.047(1)
a (Å)	5.4524(1)	5.4401(1)	5.4257(1)	5.3918(1)	5.3515(1)	5.2945(1)
b (Å)	—	—	5.3979(1)	5.4029(1)	5.4264(1)	5.4681(1)
c (Å)	13.1572(2)	13.1446(3)	7.6405(2)	7.6189(2)	7.5892(1)	7.5404(1)
V (Å^3)	225.83(4)*	224.59(5)*	223.77(4)	221.95(4)	220.38(4)	218.30(3)
wR_p	13.6	15.3	14.7	16.0	15.8	14.7
χ^2	6.5	7.5	6.2	6.6	6.1	5.1
R_B	3.6	4.2	5.2	5.5	5.2	4.7

Note. For rhombohedral samples ($x < 0.4$; $Z = 6$) rare-earths are placed at $6a$: (0, 0, 1/4), Ni at $6b$: (0, 0, 0) and O at $18e$: (x, 0, 1/4). For orthorhombic samples ($x \geq 0.4$; $Z = 4$) rare-earth are located at $4c$ (x, y, 1/4); nickel at $4b$ (1/2, 0, 0) and there are two nonequivalent positions for oxygen atoms: O (I) at $4c$ and O (II) at $8d$ (x, y, z). *Reduced volume for 4 unit formula per unit cell.

When La is replaced by Eu, a transformation is expected from a metallic state (nonlocalized magnetic moments) to localized Ni^{3+} spins.

The total susceptibility of the system [$\chi^*(T)$], taking account the different contributions, can be expressed as

$$\chi^*(T) = \chi_{core} + x\chi_{VV}^{Eu^{3+}} + \chi^{Ni}. \qquad [2]$$

The first term is the diamagnetic contribution of the atomic cores; its value was estimated to be -67×10^{-6} emu/mol for these pervskites. The second term represents the Van Vleck susceptibility of the x paramagnetic Eu^{3+} ions, and the last is the susceptibility of the magnetic Ni lattice. In the metallic cases (lower x or europium substitution) these are expected a constant value due to Pauli (χ_{Pauli}) and Landau

TABLE 2
Interatomic Ni–O Distances, Tolerance Factor and Ni–O–Ni Angle for La$_{1-x}$Eu$_x$NiO$_3$ at Room Temperature

x:	0	0.2	0.4	0.6	0.8	1
Space group:	R-3c	R-3c	Pbnm	Pbnm	Pbnm	Pbnm
Ni–O(I)						
No 2	1.934(3)	1.934(4)	1.938(3)	1.932(3)	1.949(2)	1.938(2)
Ni–O(II)						
No. 2	—		1.851(10)	1.992(3)	1.999(2)	2.010(2)
No. 2	—		2.035(10)	1.919(3)	1.910(7)	1.931(5)
$\langle$Ni–O$\rangle$	1.934(3)	1.934(4)	1.941(8)	1.948(6)	1.953(7)	1.960(5)
t^*	0.994(3)	0.992(4)	0.930(3)	0.914(3)	0.890(4)	0.885(4)
Ni–O(I)–Ni						
No. 2	165.1(2)	163.8(6)	160.5(8)	160.9(7)	153.4(6)	153.3(5)
Ni–O(II)–Ni						
No. 4	—	—	160.0(16)	154.8(10)	154.2(13)	149.9(10)
$\langle$Ni–O–Ni$\rangle$	165.1(2)	163.8(8)	160.2(16)	156.8(10)	153.9(12)	151.0(9)

*Tolerance factor is calculated as $t = \langle d_{R-O} \rangle / \sqrt{2} \langle d_{Ni-O} \rangle$. (Parenthesis show the error.)

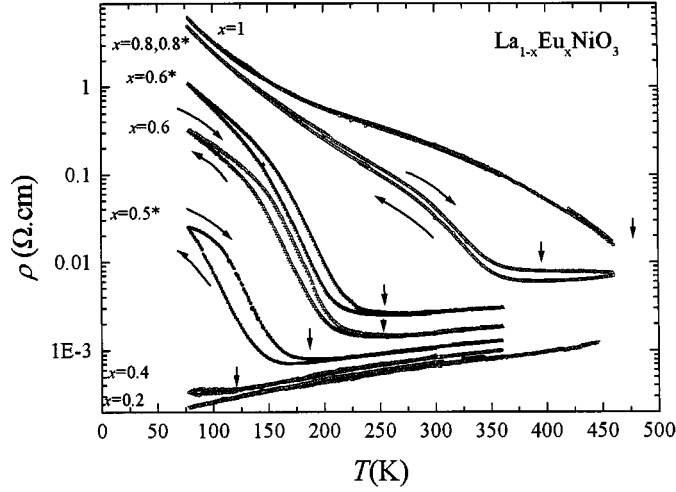**FIG. 3.** Resistivity versus temperature for the $La_{1-x}Eu_xNiO_3$ series with x = 0.2, 0.4, 0.5, 0.6, 0.8, and 1 (Series B). Samples of Series A without Gd are marked with asterisks. For $x \geq 0.4$, Eu doping shifts the metal insulator transition at high temperatures (down arrows) and decreases the hysteresis can be seen. Data collected during the cooling and heating processes are indicated in the plot. To appreciate the similar behavior, the data for the $x = 0.6*$ sample (filled triangles) were displaced with respect to $x = 0.6$. The sample with $x = 0.8*$ is similar to $x = 0.8$.

(χ_{Landau}) susceptibilities and also a quadratic dependence at high temperature according to metallic Stoner susceptibility:

$$\chi^{Ni} = \chi_{pauli} + \chi_{Landau} - aT^2 \qquad [3]$$

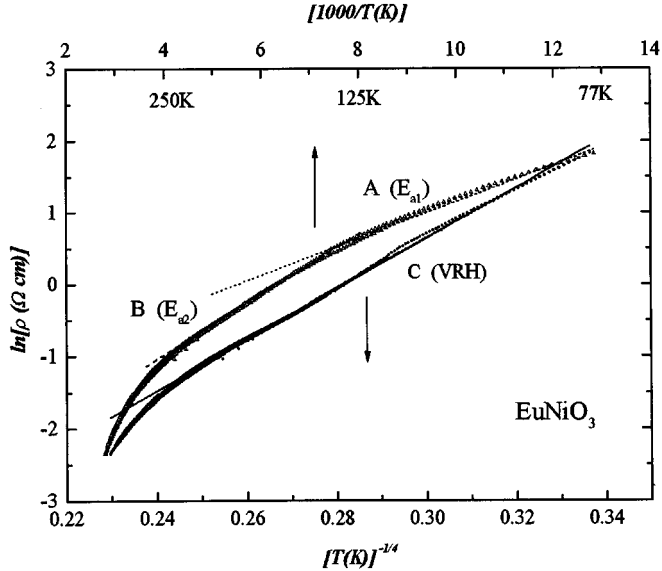[i.e., see for $x = 0.2$, Table 3 of this work and Refs. (1, 11)].

FIG. 4. Natural logarithm of electrical resistivity versus $T^{-1/4}$ (bottom axis) and versus T^{-1} (top axis) for the $x = 1$ sample. Using Eq. [1] with $f(T) = 1$, lines A and B are fits assuming an activation process ($p = 1$) at low and high T. Line C is the fit to Eq. [1] with $p = 1/4$ (VRH). To fit high-temperature data a metallic contribution must be added to this equation.
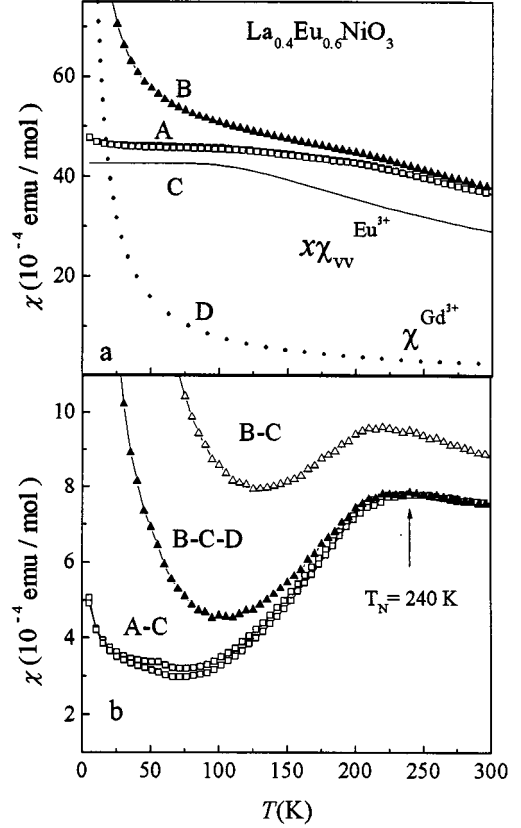

FIG. 5. (a) Total dc magnetic susceptibilities (χ^*) as a function of temperature in $La_{1-x}Eu_xNiO_3$ with $x = 0.6$. Open squares show Series A, and filled triangles, Series B. The solid line (C) is the magnetic Eu^{3+} contribution according to Eq. [4]. (b) Magnetic susceptibility estimated for the Ni lattice ($\chi^* - x\chi_{VV}^{Eu^{3+}}$) is shown for Series A in open squares and for Series B in open triangles. Filled triangles show the subtracted paramagnetic contribution of Gd^{3+} in Series B.

In the other extreme of the solution, at higher x values where the localization of Ni spins occur, Curie–Weiss behavior [$\chi^{Ni} = C/(T - \Theta)$] is expected.

The high paramagnetic contribution of the Eu ion strongly screens Ni susceptibility. Torrance *et al.* (2) determined the T_N for $EuNiO_3$ as 205 K, by measuring the paramagentic fraction by μ^+-sr (muon-spin relaxation) (8) technique. From dc magnetization experiments the Eu^{3+} susceptibility must be subtracted carefully from $\chi^*(T)$ to obtain χ^{Ni}.

The early Van Vleck work (12) considered a complete description of paramagnetic behavior:

$$\chi_{VV} = \frac{N\sum_j \{[\mu_B^2 g^2 J(J+1)/3kT] + \alpha(J)\}(2J+1)e^{-E_J^0/kT}}{\sum_j (2J+1)e^{-E_J^0/kT}}$$

$$[4]$$

where

$$\alpha(J) = \frac{\mu_B^2}{6(2J+1)}\left[\frac{f(J)}{\Delta E_{J-1;J}} + \frac{f(J+1)}{\Delta E_{J+1;J}}\right] \qquad [5]$$

$$f(J) = J^{-1} \cdot [(S+L+1)^2 - J^2] \cdot [J^2 - (S-L)^2]. \qquad [6]$$

The electronic configuration of Eu^{3+} is a singlet ground state $^7F_0$, above this a triplet free ionic state $^7F_1$ at ~ 300 cm^{-1} ($\Delta E_{01}/k_B \approx 436$ K) and at approximately 900 cm^{-1} ($\Delta E_{12}/k_B \approx 1307$ K) another level $^7F_2$. We used these values in Eq. [4] and we obtained the particular expression used for other compounds (13) with paramagnetic Eu^{3+} ions:

$$\chi_{VV}^{Eu^{3+}} = \frac{0.1241}{yT} \frac{[24 + (13.5y - 1.5)e^{-y} + (67.5y - 2.5)e^{-3y} + (189y - 3.5)e^{-6y} + \cdots]}{[1 + 3e^{-y} + 5e^{-3y} + 7e^{-6y} + \cdots]} \qquad [7]$$

with $y = 418/T$.

In Fig. 5a are the experimental data on susceptibility (Series A: La$_{1-x}$Eu$_x$NiO$_3$, Series B: La$_{1-x}$Eu$_{x-0.01}$Gd$_{0.01}$NiO$_3$) and the calculated contribution of the x Eu^{3+} present in the system. Below are plotted the subtracted Van Vleck susceptibility for both series of data. Triangles show Series B before (open) and after (fill) subtraction of the Gd^{3+} paramagnetic contribution ($\chi^{Gd^{3+}} = xC/T = 0.01 \times 7.869/T$).

In this way, we determined the Nèel temperature of the La$_{1-x}$Eu$_x$NiO$_3$ compounds (see the maximum susceptibilities in Fig. 6). Our observations are in accord with the Torrance phase diagram results (2); an increase in T_N is observed for larger values of t.

Also, Fig. 6 can be seen the hysteretic behavior of the magnetization when the sample is increasing or decreasing in temperature. This hysteresis, like that observed for electrical resistivity, indicates that a first-order phase transition takes place.

In Series B, where an extra $\chi^{Gd^{3+}}$ is present in all cases, subtraction of this gave essentially the same results as ob-tained for Series A. An extra paramagnetic tail can be observed at low temperatures in both series; the origin is not clear.

For $x = 0.4$ and 0.2, the maximum occurs at approximately the metal–insulator transition temperature (125 and ≈ 40 K).

At high temperatures, above the magnetic transition, we plot in Fig. 7 the contribution of the Ni lattice to dc magnetic susceptibility for intermediate doping of x in La$_{1-x}$Eu$_x$NiO$_3$. From the data it can be seen that the localization of the moments increases with Eu doping. Pauli–Stoner behavior evolves to a paramagnetic Curie–Weiss susceptibility (Table 3). In the inset is the inverse of the susceptibility for $x = 1$. A small change can be observed at the temperature where the metal–insulator transition occurs.

d. EPR Results

In the B-series samples, 1% Gd replaced rare-earth ions (La/Eu) as a probe for EPR experiments. At room temperature a broad line with peak-to-peak derivative linewidth $\Delta H_{pp} \approx 1500$ Oe and centered at $g \approx 2.0$ is observed for all samples. Some extra peaks are also visible, better resolved in the low-field region of the spectrum.

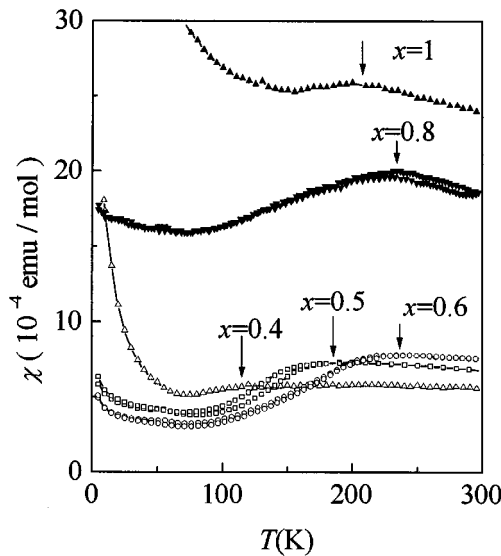In a nonmagnetic lattice the EPR spectrum of Gd^{3+} is formed by several lines due to the interaction between the

FIG. 6. Magnetic susceptibilities [$\chi_{Ni}(T)$] of the Ni lattice in the La$_{1-x}$Eu$_x$NiO$_3$ compounds for different x values. The arrows show the Nèel temperatures.
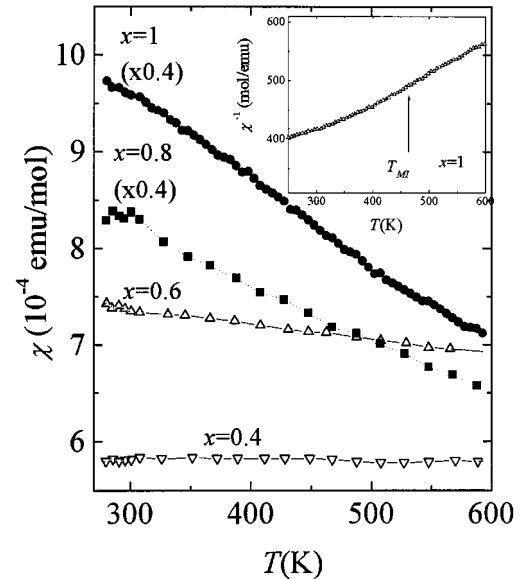

FIG. 7. High-temperature results of the magnetic susceptibility of the Ni lattice as a function of temperature. Increases in the localization of the Ni moments are seen Inset: inverse of χ_{Ni} for $x = 1$.

TABLE 3
Fit Parameters to Eq. [2], $\chi^*(T) = \chi_0 - aT^2 + C/(T-\theta)$ in the Metallic and Paramagnetic Range Temperature (ΔT)

x	ΔT (K)	χ_0 (10^{-4} emu/ mol·Oe)	A (10^{-10} emu/ mol·Oe·K^2)	C (emu·K/ mol·Oe)	θ (K)
1	480–600	—	—	2.3(1)	−680(8)
0.8	300–600	—	—	2.1(1)	−720(8)
0.6	300–600	7.0(2)	—	—	—
0.4	200–600	5.8(2)	—	—	—
0.2	80–600	10.9(3)	13.5(7)	—	—
0	5–600	5.6(2)	2.8(6)	—	—

Gd magnetic moments and the crystal field. The magnetic field position of the lines depends on the crystalline axis orientation. Since our samples are polycrystalline powders a superposition of spectra from all possible orientations is expected. Theoretical simulations superimposing the different resonance lines have been previously reported for Gd^{3+} ions occupying sites with cubic and orthorhombic symmetries (14). For orthorhombic symmetry the spectrum can be described by the spin Hamiltonian

$$\mathcal{H} = g\mu_B \mathbf{H} \cdot \mathbf{S} + \frac{D}{3} O_2^0(S) + E O_2^2(S)$$

$$+ \text{ fourth- and six-degree terms}, \qquad [8]$$

where the first term accounts for the Zeeman energy, and $O_2^0(S) = [3S_z^2 - S(S+1)]$ and $O_2^2(S) = [S_+^2 + S_-^2]/2$ are Stevens operators describing the crystal-field interaction. According to this Hamiltonian the powder spectrum for Gd^{3+} ($S = 7/2$) will consist of seven resonance lines. One intense and almost isotropic line in the center of the spectrum results from the $-1/2 \to +1/2$ transition. In addition, there will be three statellite lines on each side of it, which correspond to the $\pm 7/2 \to \pm 5/2$, $\pm 5/2 \to \pm 3/2$, and $\pm 3/2 \to \pm 1/2$ transitions. The position of these lines is associated with the divergences of the probability distributions of finding a resonance between H and $H + \delta H$. If the crystal-field interaction is small relative to the Zeeman energy, first-order perturbation theory is sufficient and second-order terms may be neglected. In our case, however, these terms give rise to an observed splitting of the central line corresponding to the $-1/2 \to +1/2$ transition with a separation (δH_0) proportional to $D^2/g\mu_B H_0$, H_0 being the central field. In the simplest case of axial symmetry ($E \cong 0$ in Eq. [8]), three pairs of satellites are expected and the lines splitting in each pair are $6D$, $4D$, and $2D$, respectively. EPR data for $La_{1-x}Gd_xNiO_3$ ($x = 0.1, 0.05, 0.01$) have been reported (10). In this case the determination of D as a function of x is unlikely because of the line broadening as a consequence of the interaction between the Gd ions.

In Fig. 8 are shown the spectra measured at $T \approx 4$ K for all samples studied. It can be seen that the intensity of the lines decreases with x, increasing the ratio of noise to signal. Arrows indicate the satellite lines that are very well observed in the case of $x = 0$ shown in Fig. 9. In Fig. 10 the positions of the satellites and of the lines corresponding to the $1/2 \to -1/2$ transitions are shown as a function of Eu content. A value of $D/k_B \cong 0.18(2)$ K can be estimated that results independently of x. A similar D value was found for Gd in the perovskite-related superconductor $EuBa_2Cu_3O_{3-\delta}$ (14).

When the temperature is increased the resolution of the spectra deteriorates but the position of the visible satellites remains constant. For larger Eu concentrations, variations in intensity, g factor, and linewidth are observed in the high-temperature regime ($T \geq 200$ K). It is not possible to relate these changes only to the AF–PM transition because similar effects are observed in other compounds (15) as a consequence of the existence of a magnetic level in Eu^{3+} or Sm^{2+} at $\Delta E_{01}/k_B \approx 436$ K.

The most obvious changes in the spectrum at 4 K on going from x = 0 to x = 1 are the decrease in intensity and growth of a narrow line at $g \approx 2$ (see Fig. 8). Spectra with well-resolved satellite lines are found for $x = 0$ and $x = 0.2$ ($t > 0.93$). An important decrease in the spectrum intensity is observed for samples with $t \leq 0.93$. For $x = 0.4$ and 0.6,
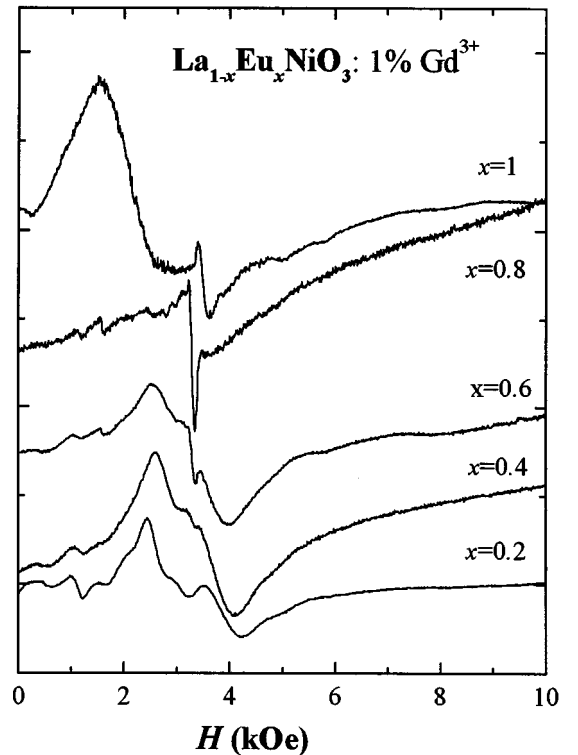

FIG. 8. ESR spectra of Gd^{3+} in $La_{1-x}Eu_xNiO_3$: Gd^{3+} taken at liquid helium temperature. The x values are indicated in the plot.
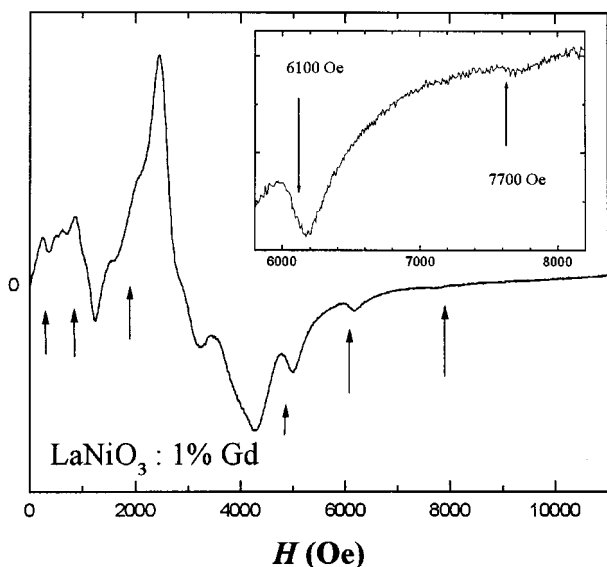
FIG. 9. ESR spectrum of Gd^{3+} in the $x = 0$ member of the La$_{1-x}$Eu$_x$NiO$_3$: Gd^{3+} series at liquid helium temperature. Inset: details of the spectrum.

although less intense, the central line corresponding to the $-1/2 \rightarrow +1/2$ transition is still visible. For samples with larger Eu concentration the spectrum shows the major changes: for $x \geq 0.8$ the central line disappears and for $x = 1$ a second very intense resonance is observed centered at lower fields (Fig. 8).

In Refs. (5, 6) complete magnetization of the Ni sublattice at 4 K was reported for PrNiO$_3$, NdNiO$_3$, SmNiO$_3$, and EuNiO$_3$. The magnetic moment for $T \rightarrow 0$ is $0.9\mu_B$, except for EuNiO$_3$ where it is $1.2\mu_B$. In all cases the results were interpreted considering a Ni orbital ordering and two different sites for the rare-earth ion. One site corresponds to $B^{\pm}$ planes where the net exchange field created by the eighth Ni nearest neighbor is nonnull and the second to B^0 planes where the expected exchange field is 0 or vanishing small. Long-range order in the rare-earth sublattice was found for Nd and Sm cases at $T < 50$ K. The tolerance factors of our samples are similar to those in (5, 6): $t(x = 0.4) = t(\text{NdNiO}_3) < t(x = 0.6) < t(\text{SmNiO}_3) < t(x = 0.8) < t(\text{Eu-NiO}_3 \text{ or } x = 1)$. Is only the tolerance factor important for the magnetic properties of these compounds? If this is true the magnetic state should be the same for $x \geq 0.4$ except, perhaps, for some larger magnetization in the Eu-rich samples.

It was observed that when almost all the rare-earth sites are occupied by La and the Ni sublattice is not magnetized, the Gd spectrum is that corresponding to the crystal-field interaction described above. In the other limit, for $x = 1$, the intense and broad line displaced from $g = 2$ can be associated with the presence of an effective field in the Gd sites (B$^{\pm}$ planes) produced by the Ni sublattice magnetization.

Similar behavior, attributed to Cu ordering, was reported for Gd$_2$CuO$_4$ (16). However, even in the $x = 1$ case, a small line at $g = 2$ (see Fig. 8) is still observed and would correspond to Gd ions that are not affected by any effective field (B^0 planes). In the intermediate cases, with the Ni sublattice magnetized, the crystal-field spectrum is still visible but it is progressively lost while the Eu concentration increases. In Refs. (5, 6) an increase in the covalence of Ni–O bonding due to the presence of Eu was reported. In this case, one expects weaker Gd–O bonding for Gd ions that are near neighbors of Eu. It is a possible explanation for the intensity decrease. However, it is also possible that an increasing number of different types of Gd sites, with some different symmetry, were the cause of the experimental observations.

4. DISCUSSION AND CONCLUSIONS

The thermal hysteresis observed in the electral properties of these compounds (La$_{1-x}$Eu$_x$NiO$_3$) is also observed in other families, like PrNiO$_3$ (17) and NdNiO$_3$ (18), and can be attributed to a first-order transition (electrical inhomogeneities due to a slow change between the metal and the semiconducting phases). When samples cool down, electrons become gradually localized creating some insulating zones. When the sample is heated, some electrons are able to reach the conduction band. Then, the "percolation point" varies on heating or cooling the sample. In that way, while thermal hysteresis is observed, there is a mixture of insulating and metallic phases.

For a general view of the metal–insulator transition when Eu^{3+} is replaced by La^{3+}, the system can be described in terms of the relative energies of three electronic energy states near the Fermi level, following the ZSA model (19). The
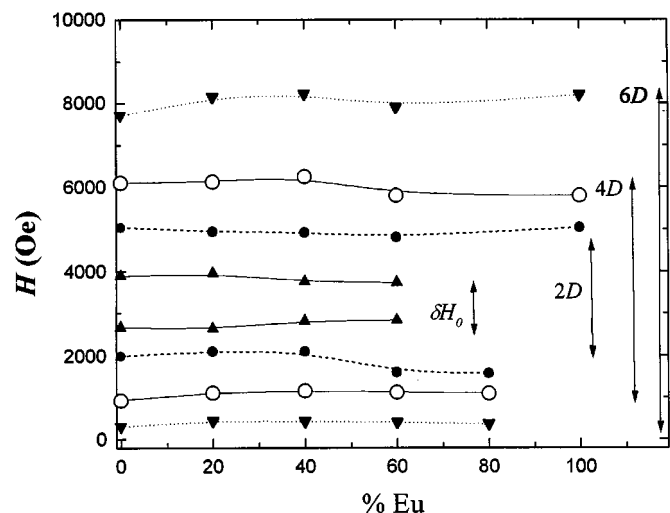

FIG. 10. Position of the resonance lines for the La$_{1-x}$Eu$_x$NiO$_3$: Gd^{3+} series as a function of %Eu (or x).

$RNiO_3$-type oxides are included in the charge transfer insulator compounds (20). For a charge transfer insulator, the fully occupied oxygen $2p$ state lies at an energy Δ under the unoccupied metal orbital and at an energy $(U\text{-}\Delta)$ over the highest occupied metal orbital. The gap is dominated by the value of Δ. The metallic behavior of these samples (and the temperature for the M–I transition) corresponds to the closing of this gap. In Table 4 we present the Ni–O–Ni angle and metal–insulator transition temperature for each compound in the series.

For high values of the angle, the $2p$ oxygen band and the $3d$ Ni band overlap, and the compound is metallic. On decreasing the Ni–O–Ni angle, the $2p$ oxygen band narrows, causing the insulating state.

This Ni–O–Ni angle also tends to straighten out as the temperature is increased; this effect has been measured in $PrNiO_3$ by Huang *et al.* (21), who found that it increases by $1.5°$ approximately between 300 and 673 K. The only structural change in the insulator–metal transition appears to be the change in unit-cell volume, which can be quantitatively accounted for by means of a decrease in the Ni–O bond length induced by electronic delocalization. The insulator–metal transition in these compounds is not complicated by structural changes and therefore there are a range of temperatures and tolerance factors across which this angle, and, therefore, electronic bandwidth, vary gradually. As the tolerance factor increases (or the relative Eu/La concentration diminishes) the bandwidth increases and the compounds become more metallic.

In summary, $La_{1-x}Eu_xNiO_3$ shows, with increasing x, a sharp first-order metal–insulator transition with thermal hysteresis, a decrease in the hysteresis width, a shift to high temperature of T_{M-I} and a polaronic conduction influenced by disorder in the high-resistivity Eu composition. Also, the magnetic ordering temperature (T_N) strongly depends on the rare-earth ion occupying the space between octahedra. Both characteristic temperatures are shown as a function of the tolerance factor in Fig. 11. This phase diagram can be
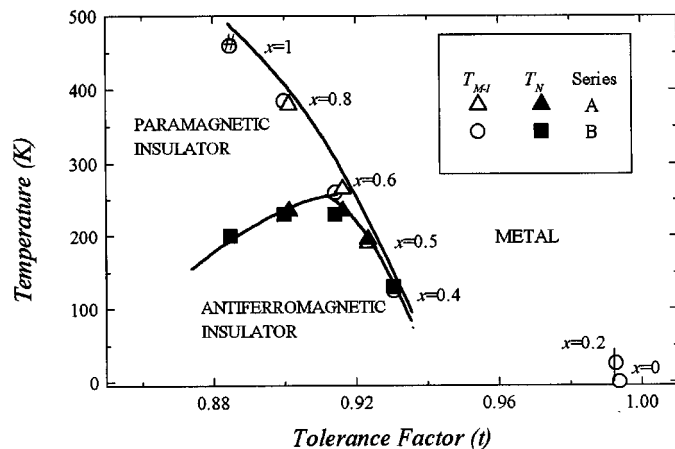

FIG. 11. Phase diagram of $La_{1-x}Eu_xNiO_3$ obtained from crystallographic, magnetic, and electrical data.

related to the closing of a charge-transfer gap. The variations in the Ni–O–Ni angle determine the bandwidth and then the T_{M-I}. However, the paramagnetic tail at low temperatures and the disorder in the semiconducting region observed could be associated with small amounts of Ni^{2+} ($S = 1$) coming from a disproportionation of Ni^{3+}.

EPR spectroscopy using Gd ions as a probe has been shown to be a valuable technique in studying this family of compounds. For a full understanding of the observations, however, it will be necessary to extend the study to other rare-earth nickelates with similar tolerance factors. The main result is that, at least at the Gd sites, the average crystal-field characteristics do not change with x. However, an increasing number of Gd ions stop contributing to the crystal-field spectrum when Eu doping increases. This could be a consequence of the increase in Ni–O covalence in the neighborhood of the Eu sites.

TABLE 4
Variation of the Ni–O–Ni Angle, Metal–Insulator Transition Temperature (T_{M-I}) and Antiferromagnetic Order Temperature (T_N) with Europium Content. (*Estimated temperature, #taken from (8))

%Eu (x)	⟨Ni–O–Ni⟩ (deg)	T_{M-I} (K)	T_N (K)
0	165.1(2)	Metallic	—
20	163.8(8)	30*	40(5)
40	160.2(16)	125(2)	120(5)
50	158.5(13)	190(2)	190(5)
60	156.8(10)	260(2)	235(5)
80	153.9(12)	380(2)	235(5)
100	151.0(9)	460#	200(5)

REFERENCES

1. R. D. Sánchez, M. T. Causa, J. Sereni, M. Vallet-Regí, M. J. Sayagués, and J. M. González-Calbet, *J. Alloys Compd.* **191**, 287 (1993).
2. J. B. Torrance, P. Lacorre, A. I. Nazzal, E. J. Ansaldo, and Ch. Niedermayer, *Phys. Rev. B* **45**, 8209 (1997).
3. M. Medarde, P. Lacorre, K. Conder, F. Fauth, and A. Furrer, *Phys. Rev. Lett.* **80**, 2397 (1998).
4. J. A. Alonso, J. L. García Muñoz, M. T. Fernandez-Díaz, M. A. G. Aranda, M. J. Martinez-Lope, and M. T. Casais, *Phys. Rev. Lett.* **82**, 3871 (1999).

5. J. L. García Muñoz, J. Rodríguez Carvajal, P. Lacorre, *Phys. Rev. B* **50,** 978 (1994); J. L. García Muñoz, P. Lacorre, and R. Cywinski, *Phys. Rev. B* **51,** 15197 (1995).

6. J. Rodríguez Carvajal, S. Rosenkranz, M. Medarde, P. Lacorre, M. T. Fernández Díaz, F. Fauth, and V. Trounov. *Phys. Rev. B* **57,** 456 (1998).

7. J. Blasco M. Castro, and J. Garcia. *J. Phys. Condens. Matter* **6,** 5875 (1994).

8. J. A. Alonso, M. J. Martinez-Lope, and I. Rasines, *J. Solid State Chem.* **120,** 170 (1995).

9. M. L. Medarde, *J. Phys. Condens. Matter.* **9,** 1679 (1997).

10. R. D. Sánchez, M. T. Causa, A. Caneiro, A. Butera, M. Vallet-Regí, M. J. Sayagués, J. González-Calbet, F. García-Sanz, and J. Rivas, *Phys. Rev. B* **54,** 16574 (1996).

11. R. D. Sánchez, F. García-Sanz, J. Rivas, and M. T. Causa, *J. Alloys Compd.* **239,** 31 (1996).

12. J. H. Van Vleck, *Phys. Rev.* **31,** 587 (1928).

13. A. Frank, *Phys. Rev.* **39,** 119 (1932).

14. M. T. Causa, C. Fainstein, G. Nieva, R. Sánchez, L. B. Steren, M. Tovar, R. Zysler, D. C. Vier, S. Schultz, S. B. Oseroff, Z. Fisk, and J. L. Smith, *Phys. Rev. B* **38,** 257 (1988), and references therein.

15. F. Mehran, K. W. H. Stevens, and T. S. Plaskett, *Phys. Rev. B* **20,** 1817 (1979), and references therein.

16. A. Butera, A. Caneiro, M. T. Causa, L. B. Steren, R. Zysler, M. Tovar, and S. B. Oseroff, *Physica C* **160,** 341 (1989).

17. X. Q. Xu, J. L. Peng, Z. Y. Li, H. L. Ju, and R. L. Greene, *Phys. Rev. B* **48,** 1112 (1993).

18. J. Perez, J. Stankievwicz, J. Blasco, M. Castro, and J. García, *J. Phys. Condens. Matter* **8,** 10393 (1996).

19. J. Zaanen, G. A. Sawatzky, and J. W. Allen, *Phys. Rev. Lett.* **55,** 418 (1985); J. Zaanen and G. A. Sawatzky *J. Solid State Chem.* **88,** 8 (1990).

20. J. A. Alonso, M. J. Martinez-Lope, and M. A. Hidalgo, *J. Solid State Chem.* **116,** 146 (1995).

21. T. C. Huang, W. Parrish, H. Toraya, P. Lacorre, and J. B. Torrance, *Mater. Res. Bull.* **25,** 1091 (1990).